

RESEARCH ARTICLE | MAY 23 2025

Electron charge dynamics in metal-dot QCA cell using gate reflectometry

Alexei O. Orlov ; Mohammad Istiaque Rahaman ; Géza Tóth ; Gergo P. Szakmany ;
Xavier Jehl ; Jonathan D. Chisum ; Craig S. Lent ; Gregory L. Snider 



APL Electronic Devices 1, 026116 (2025)

<https://doi.org/10.1063/5.0271627>

 CHORUS



Articles You May Be Interested In

Measurements of variable capacitance using single port radio frequency reflectometry

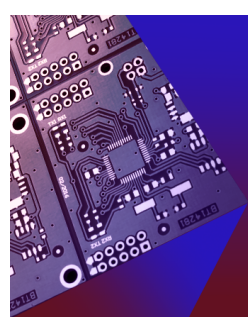
Rev. Sci. Instrum. (August 2023)

Using single-electron box arrays for voltage sensing applications

Appl. Phys. Lett. (May 2020)

Radio-frequency reflectometry on an undoped AlGaAs/GaAs single electron transistor

Appl. Phys. Lett. (January 2014)



APL Electronic Devices

Fostering connections across multiple disciplines
in the broad electronics community

Now Open for Submissions



Electron charge dynamics in metal-dot QCA cell using gate reflectometry

Cite as: APL Electron. Devices 1, 026116 (2025); doi: 10.1063/5.0271627

Submitted: 19 March 2025 • Accepted: 8 May 2025 •

Published Online: 23 May 2025



View Online



Export Citation



CrossMark

Alexei O. Orlov,^{1,a)} Mohammad Istiaque Rahaman,¹ Géza Tóth,^{2,3} Gergo P. Szakmany,¹ Xavier Jehl,⁴ Jonathan D. Chisum,¹ Craig S. Lent,¹ and Gregory L. Snider¹

AFFILIATIONS

¹ Department of Electrical Engineering, University of Notre Dame, Notre Dame, Indiana 46556, USA

² Department of Theoretical Physics, University of the Basque Country, Leioa, Spain

³ IKERBASQUE, Basque Foundation for Science, Bilbao, Spain

⁴ University Grenoble Alpes, CEA, Grenoble INP, IRIG, PHELIQS, Grenoble, France

^{a)} Author to whom correspondence should be addressed: aorlov@nd.edu

ABSTRACT

Quantum-dot cellular automata (QCA) is a field-coupled computational paradigm [C. S. Lent *et al.*, *Nanotechnology* **4**, 49 (1993)] that encodes binary information through the positions of single electrons within quantum-dot cells. In this work, we present experimental results obtained using RF gate reflectometry on two coupled floating metal double dots (DDs). We demonstrate that a single gate sensor can effectively capture the behavior of both DDs, providing detailed insights into their charging dynamics. The observed variations in the reflected signal directly correspond to changes in electron tunneling rates. Experiments reveal that at low temperatures ($T \approx 0.35$ K), tunneling within DDs in the non-polarized state of a QCA cell becomes strongly correlated, leading to low-frequency (≤ 30 kHz) thermally driven random fluctuations in cell polarization. However, the cell remains capable of fast and robust switching when driven by an input signal. Furthermore, we provide the first direct experimental measurement of temperature effects on QCA switching. At elevated temperatures, where the Coulomb blockade is weakened, we observe degradation in the abruptness of the switching, which could lead to signal loss across a chain of cells unless appropriate clocking mechanisms are implemented.

© 2025 Author(s). All article content, except where otherwise noted, is licensed under a Creative Commons Attribution-NonCommercial 4.0 International (CC BY-NC) license (<https://creativecommons.org/licenses/by-nc/4.0/>). <https://doi.org/10.1063/5.0271627>

04 August 2025 18:38:19

Quantum-dot cellular automata (QCA)^{1,2} utilizes the position of single electrons within cells composed of four quantum dots arranged in a square and charged with two electrons to represent binary information—replacing traditional transistor-based circuits. Due to the Coulomb interaction, the two electrons naturally occupy diagonally opposite dots. The configurations of the electrons within the cell are used to encode “0” or “1.” Computation in QCAs is driven by electrostatic interactions between neighboring cells rather than current flow, enabling ultra-low power and high-density circuits. One possible implementation of a QCA cell, shown in Fig. 1(a), is composed of two capacitively coupled double-dots (DDs), where electron tunneling is allowed between $D_1 - D_2$ and between $D_3 - D_4$. The movement of electrons in DDs is governed by the Coulomb blockade³ at operating temperature $k_B T \ll E_C$, where $E_C = e^2/2C_{DD}$ is the charging energy of the DD with a total capacitance of C_{DD} .

Here, k_B is the Boltzmann constant, T is the temperature, and e is the electron charge.

When no bias is applied to the gates, the cell remains charge-neutral and electron transport is suppressed by the Coulomb blockade. To facilitate QCA operation, electron movement within the DDs must be enabled by lifting the Coulomb blockade by voltage application to gates G1–G4. The subsequent application of a small differential bias to the input gates (either G1-G2 or G3-G4 can be used as inputs) at low temperature, $k_B T \ll E_C$, results in single electrons being “frozen” in diagonally opposing dots of the cell leading to cell polarization, defined by the polarity of the applied input bias. However, if the Coulomb blockade is lifted but no differential bias is applied, the cell stays in the non-polarized (NP) state. In this state, electrons randomly tunnel within each DD, causing fluctuations in cell polarization. Yet, due to mutual electron repulsion,

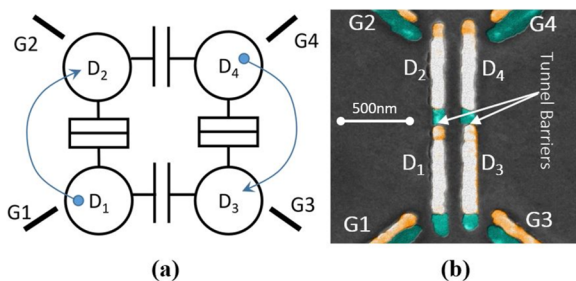


FIG. 1. (a) QCA cell composed of four dots. Electrons (blue dots) can tunnel between D_1 and D_2 , and between D_3 and D_4 . Dots D_1 to D_3 and D_2 to D_4 are electrostatically coupled. (b) High-resolution electron micrograph of the device.

random electron motion becomes correlated, significantly reducing tunneling rates and, consequently, the frequency of these fluctuations. In early experiments,^{4,5} low-frequency differential conductance was measured simultaneously in two electrostatically coupled DDs, revealing a substantial conductance reduction when both DDs were in the NP state.

When the Coulomb blockade is lifted, the tunneling rate, Γ_t , within a standalone DD is determined by the junction resistance R_j and temperature T , as introduced in Ref. 6: $\Gamma_t = k_B T / e^2 R_j$. However, when two capacitively coupled DDs form a QCA cell, Fig. 1(a), the random movement of electrons in the NP state becomes correlated. At $T \ll E_C/k_B$, the rate of these thermally driven correlated charge fluctuations can be many orders of magnitude lower than Γ_t .^{5,7}

In this work, we characterize the operation of a QCA cell, with a particular focus on tracking changes in electron tunneling rates in the non-polarized state. Our method relies on the dependence of measurable tunneling capacitances in a single-electron device on the electron tunneling rate, providing insight into the underlying charge dynamics. To probe these dynamics within a metal–oxide–metal QCA cell, we employ RF gate reflectometry. In RF gate reflectometry, a technique widely applied in metal–oxide–metal devices^{8–12} and semiconductor quantum dots,^{13–15} the admittance of gate-coupled single-electron devices is measured. When the Coulomb blockade is lifted, single electrons move within the DDs, giving rise to an additional “tunneling capacitance”^{8,16,17} due to their ability to pass through a tunnel junction. If charge transfer in the DDs is adiabatic, i.e., thermal relaxation occurs at a rate γ ⁸ faster than the probing frequency f , $\gamma > 2\pi f$, the admittance is primarily capacitive. In contrast, if $2\pi f > \gamma$, the admittance becomes predominantly resistive, corresponding to excess power dissipation due to the Sisyphus resistance effect, R_{Sis} .⁸

Variations in the experimentally obtained reflection coefficient, Γ_{ref} , directly correspond to changes in electron tunneling rates. To analyze this behavior, we perform theoretical calculations of tunneling rates in the QCA device using experimentally determined parameters as a function of gate voltages applied to G₁–G₄. Finally, by modeling gate reflectometry sensing, we evaluate how tunneling rate variations affect Γ_{ref} , enabling a direct comparison between experimental and theoretical results.

The QCA device is fabricated using the standard Niemeyer–Dolan bridge technique¹⁸ with high-resolution electron beam lithography. The detailed fabrication procedures are provided

in the [supplementary material](#), Sec. S1. A high-resolution colorized micrograph of the completed QCA device is shown in Fig. 1(b). It consists of two DDs, each formed by two elongated nanoscale metal islands separated by a tunnel junction. This design ensures tight coupling between D_1 and D_3 , as well as between D_2 and D_4 , while minimizing cross-capacitance between diagonally opposing islands (i.e., D_1 to D_4 , and D_2 to D_3). A 3D model of the cell, consisting of two tunnel junctions and non-leaky capacitors between the dots and electrodes (see Sec. S2 and Table S1 in the [supplementary material](#)), was implemented in COMSOL Multiphysics¹⁹ to simulate device operation.

In experiments, we detect single-electron charge transitions in both DDs of QCA using an RF gate reflectometry setup,¹² as shown in Fig. 2. A matching network (MN) is connected to gate G₁ to enable measurements; see Sec. S3 in the [supplementary material](#) for further details. These transitions are detected by monitoring the reflection coefficient, Γ_{ref} , of the QCA device from port G₁ as a function of the applied differential gate bias V_{IN} and set-point bias V_S .

From the perspective of port G₁, each DD can be treated as a single-electron box (SEB),²⁰ coupled to it with a strength determined by the respective equivalent coupling capacitance (Fig. S4 in the [supplementary material](#)). In the blockaded regions, charge remains “frozen,” tunneling is suppressed, and Γ_{ref} remains constant, corresponding to reflection from a static capacitive network. When the Coulomb blockade is lifted, electron tunneling within the double dot (DD) leads to observable variations in the complex admittance at port G₁ (see Sec. S4 in the [supplementary material](#)).

In this work, a single-gate RF reflectometry sensor is used to characterize the charging processes in a four-dot QCA cell. Experimental results at low temperature are presented as 2D maps of the reflection coefficient, $\Theta_{\text{ref}}(V_{IN}, V_S)$, and $|\Gamma_{\text{ref}}|(V_{IN}, V_S)$. However, at high temperatures, the $|\Gamma_{\text{ref}}|(V_{IN}, V_S)$ response becomes indistinguishable from noise, consistent with theoretical predictions, and we only present $\Theta_{\text{ref}}(V_{IN}, V_S)$ data.

The experiment is designed so that either DD can function as a “driver” to the other, Fig. 2. Consequently, two gate voltage configurations are explored: in configuration (a), V_{IN} is applied to gates G₃ and G₄, inducing single-electron transitions in D_3D_4 . This, in

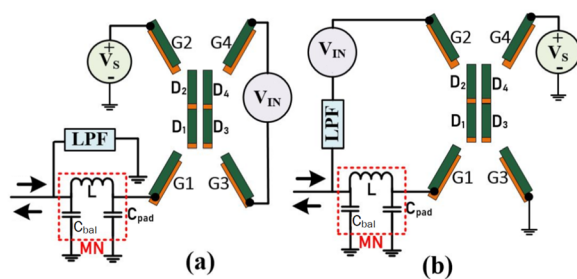


FIG. 2. Simplified circuit diagram of the experiment. Two configurations are shown. In panel (a), the application of V_{IN} to gates G₃ (+) and G₄ (−) forces electron switching in D_3D_4 ; the set point bias V_S is applied to G₂, and DC voltage at G₁ is set to 0. In panel (b), the application of V_{IN} to gates G₁ (+) and G₂(−) forces electron switching in D_1D_2 ; and the set point bias V_S is applied to G₄, and DC voltage at G₃ is set to 0. We used diplexer ZDPLX-2150-S+ from Mini-Circuits, schematically shown as a low-pass filter to split DC and RF signals.

turn, flips single electrons in D_1D_2 , which has been preset into the NP state by applying a set-point bias V_S . In configuration (b), the input bias V_{IN} switches electrons in D_1D_2 , which can subsequently cause electron switching in the opposite direction in D_3D_4 . Here, the set-point bias V_S ensures that D_3D_4 remains in the NP state (see Sec. S5 in the [supplementary material](#) for details). The experimentally obtained 2D maps of $\Theta_{ref}(V_{IN}, V_S)$ and $|\Gamma_{ref}|(V_{IN}, V_S)$ of the reflection coefficient obtained at experimental temperature of $T = 0.35$ K are presented in [Fig. 3](#) for two respective inputs of the QCA. In [Figs. 3\(a\) and 3\(b\)](#), single electrons are switched in D_3D_4 , which triggers the switching of electrons in D_1D_2 in the opposite direction. [Figures 3\(c\) and 3\(d\)](#) show the inputs and outputs reversed compared to panels (a) and (b).

The experiment reveals two distinct sets of lines with noticeably different contrast against a uniform blue background. This background represents the Coulomb-blockaded state, where electron transport is suppressed in both DDs, and $\Gamma_{ref} = \text{const}$. The lines with stronger contrast correspond to signals originating from D_1D_2 , which is directly coupled to the sensing gate G1. Each switching event in D_1D_2 induces a significant phase and magnitude deviation in the reflected signal, appearing as bright red lines. A second set of nearly perpendicular lines, exhibiting much weaker contrast—barely shifting from blue to white—arises from electron switching in D_3D_4 .

The smaller change in response results from the much weaker coupling between D_3D_4 and the sensing gate G1.

The segments connecting the closest break points on adjacent zigzagging lines (originating from signals from both DDs) define regions corresponding to the QCA NP state. A close-up view of one such region is shown in [Fig. S6\(b\)](#) (simulation) and [Fig. S6\(c\)](#) (experiment) in the [supplementary material](#). In [Figs. 3\(a\) and 3\(b\)](#), electron switching in D_3D_4 , driven by V_{IN} , triggers electron transitions in D_1D_2 , e.g., near $V_{IN} \approx 0$ mV and at a set-point bias of $V_S \approx -10$ mV. Conversely, in [Figs. 3\(c\) and 3\(d\)](#), the switching in D_1D_2 , driven by V_{IN} , induces transitions in D_3D_4 , e.g., near point $V_{IN} \approx -50$ mV and $V_S \approx -20$ mV. These regions, characterized by distinct line breaks and central voids, indicate the suppression of single-electron transport in both DDs. Note that line breaks are hallmarks of the Coulomb interaction, as observed in various spin qubit experiments.^{15,21} They result from mutual Coulomb repulsion, which inhibits electron transport in both DDs, as previously observed in DC conductance measurements of QCA.^{4,5} The strength of the coupling between the upper and lower DDs determines the magnitude of this repulsion and defines the shape of the voids. As seen in [Fig. 3](#), single-electron transport is very strongly suppressed in the voids, effectively blocking transport in both DDs. In addition, both sets of zigzagging lines appear slightly tilted, reflecting the

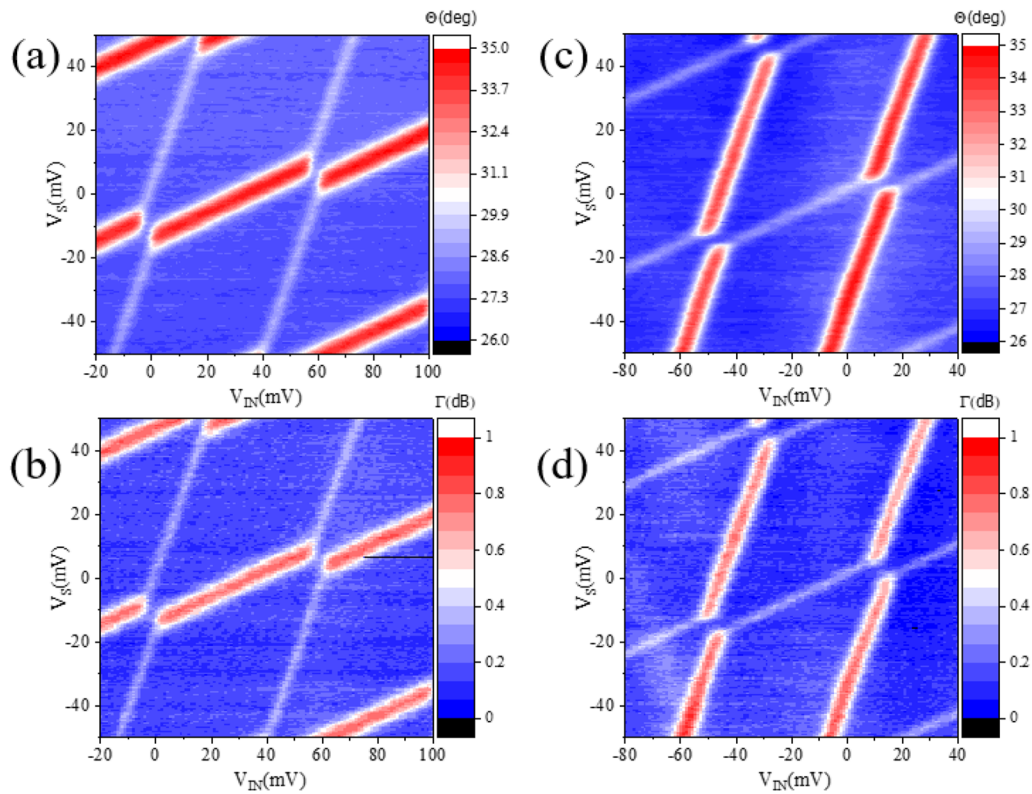


FIG. 3. Experimentally obtained maps, $\Theta_{ref}(V_{IN}, V_S)$ (a) and (c), and $|\Gamma_{ref}|(V_{IN}, V_S)$ (b) and (d) at $T = 0.35$ K: (a) and (b)—gate configuration [Fig. 2\(a\)](#); (c) and (d)—gate configuration [Fig. 2\(b\)](#).

asymmetry in capacitive coupling between the respective gates and dots (see Table S1 in the [supplementary material](#)).

The experiment is repeated at an elevated temperature $T = 2.5$ K, as shown in Fig. 4. In Fig. 4(b), the input and output terminals are swapped relative to those in Fig. 4(a).

At this temperature, the suppression of tunneling becomes nearly undetectable (i.e., the “voids” disappear and the line contrast barely changes). However, note that the offsets in the zigzag pattern remain unchanged, as they are solely determined by electrostatics. Simulations of DD charging were performed using the methods described in Refs. 5 and 7, based on Refs. 3, 6, 22, and 23. For calculations, we used the parameters of the tunnel junctions in the DD based on measurements of SETs fabricated alongside a QCA cell with identical design parameters.

Using measured charging diagrams of the SETs, we determined the charging energy as $E_C = \frac{e^2}{2(2C_j + C_g)}$, where $C_g \approx 1$ aF is a gate capacitor of the SET, from which we extracted the junction capacitance: $C_j \approx \frac{e^2}{4E_C} \approx 40$ aF. In addition, from the measured SET conductance, we estimated the junction resistance as $R_j \approx \frac{R_{\text{SET}}}{2} \approx 130$ k Ω . We first generated the relevant configurations for the metallic islands and then calculated the free energy of various configurations, which depends on the lead voltages. In our system, electrons do not tunnel out from the islands via voltage sources; thus, the tunneling rates depend only on the free energies of the initial and final configurations. The probabilities of these configurations in the steady state can be obtained from the Boltzmann distributions.

In particular, the free energy is given as

$$F = \frac{1}{2} \begin{bmatrix} q \\ q' \end{bmatrix}^T C^{-1} \begin{bmatrix} q \\ q' \end{bmatrix} - v^T q', \quad (1)$$

where C is the capacitance matrix that describes the structure of the circuit, q and q' are the island charge vector and the lead charge vector, respectively, and v is the vector of the lead voltages. The elements of q are integer multiples of the elementary charge e , while

the elements of q' can be computed based on the lead voltages, the island charges, and the capacitance matrix.²² Next, we determined the allowed transitions between configurations and obtained the tunneling rates, Γ_t , for these allowed transitions as

$$\Gamma_{t(i \rightarrow j)} = \frac{1}{e^2 R_j} \frac{-\Delta F_{ij}}{1 - e^{\Delta F_{ij}/k_B T}}, \quad (2)$$

where $\Delta F_{ij} = F_j - F_i$. Using the tunneling rates and the steady state probabilities of the configurations, we can compute the tunneling rates of electrons within the two double-dots.

Increasing the temperature of the system drastically alters the interaction between electrons in a QCA cell. As the temperature approaches $T = E_C/k_B$, the suppression of single-electron tunneling in blockaded regions decays exponentially, while electron tunneling rates increase as $\Gamma_t \propto k_B T$. This significantly weakens the correlation of electron switching in the DDs, effectively rendering QCA operation impossible.

The comparison between theory and experiment is carried out in several steps (for more details, see Sec. S6 in the [supplementary material](#)). First, we convert the calculated tunneling rates Γ_t for electrons in both DDs [Figs. S7(a) and S7(b) in the [supplementary material](#)] into admittance values, incorporating both dynamic capacitance and Sisyphus resistance effects.²⁴ Cross-sectional views of the real and imaginary components of the calculated admittance maps for non-interacting DDs are shown in Fig. S8 for two temperatures: $T = 0.35$ K (a) and $T = 2.5$ K (b). The calculated admittance values are then probed by the simulated reflectometer with parameters closely matching those of the experimentally characterized matching network. The calculated 2D maps $\Theta_{\text{ref}}(V_{IN}, V_S)$ and $|\Gamma|_{\text{ref}}(V_{IN}, V_S)$ for two experimental temperatures are presented in Fig. 5; cross-sectional views of the corresponding magnitude and phase of the reflection coefficient in non-interacting regions are presented in Fig. S9 (a: $T = 0.35$ K, b: $T = 2.5$ K).

The simulation results show excellent quantitative agreement with experimental observations at both temperatures.

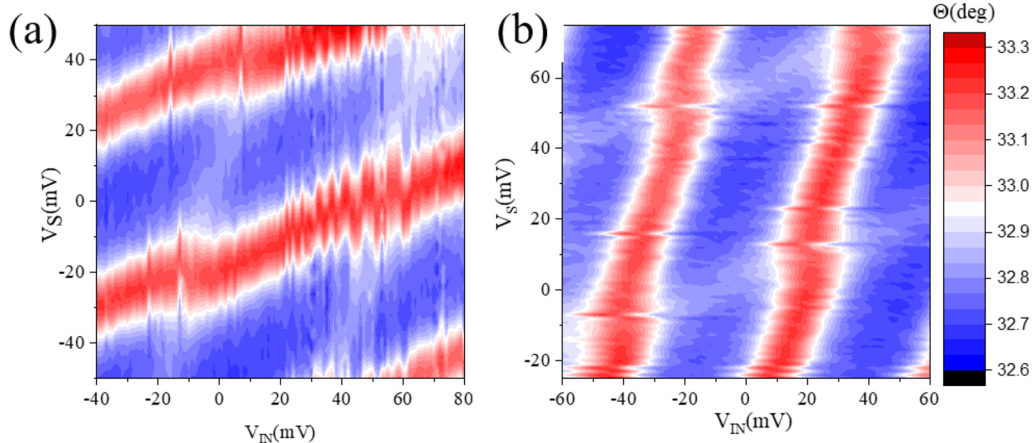


FIG. 4. Experimentally obtained maps $\Theta_{\text{ref}}(V_{IN}, V_S)$ at $T = 2.5$ K: (a) gate configuration Fig. 2(a); (b) gate configuration Fig. 2(b).

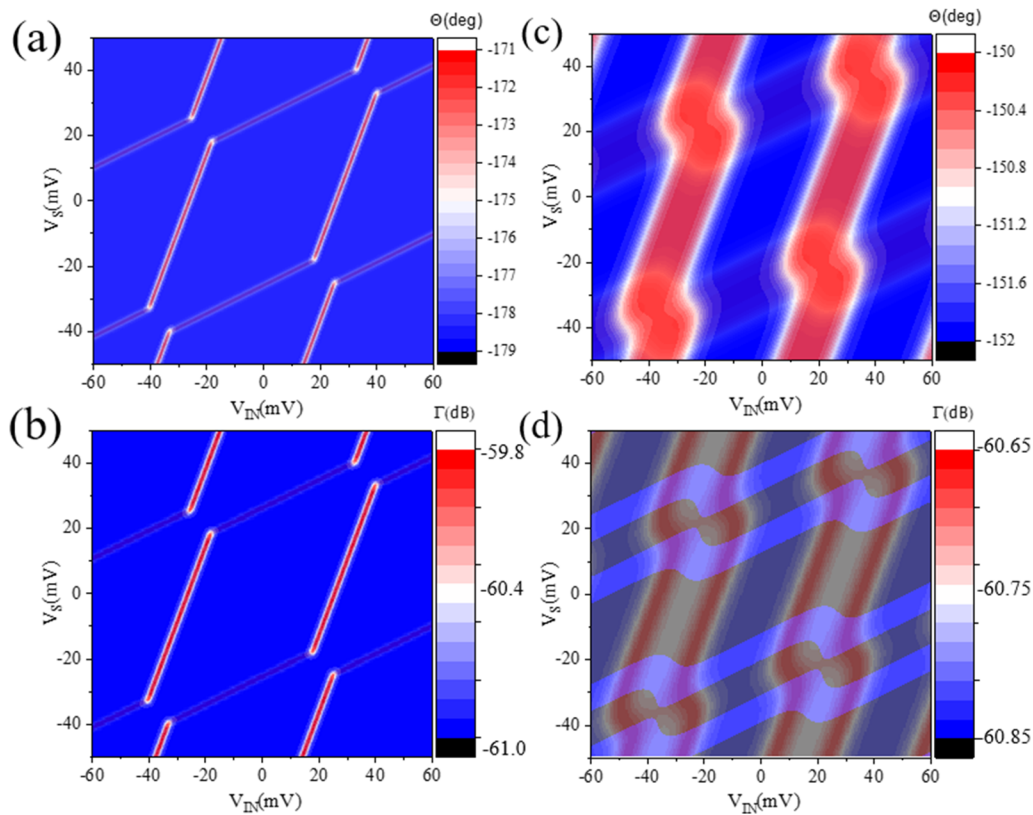


FIG. 5. Calculated plots of $\Theta_{ref}(V_{IN}, V_S)$ and $|\Gamma_{ref}|(V_{IN}, V_S)$ for (a) and (b) $T = 0.35$ K; (c) and (d) $T = 2.5$ K. Gate configuration of Fig. 2(b) is used.

In conclusion, we characterized charge dynamics in a nanoscale floating metal QCA cell using RF gate reflectometry at two temperature regimes: strong ($T \leq E_C/50k_B$) and weak Coulomb blockade ($T > E_C/10k_B$), where $E_C/k_B \approx 20$ K. For direct comparison, tunneling rates simulated using the experimental parameters of the device were translated into changes in the experimentally obtained reflection coefficient, revealing strong quantitative agreement. We emphasize that an exponentially strong suppression of electron tunneling in both DDs in the NP state is observed when $E_C \geq 50k_B T$, from ≈ 1 GHz to ≤ 30 kHz [Fig. S7(c) in the [supplementary material](#)] due to correlated electron movements in DDs.^{4,5} However, once the cell is driven (i.e., an input signal is applied), switching remains fast and robust. In addition, both experimental and simulated data indicate that at elevated temperatures ($T \approx E_C/8k_B$), the reduction in tunneling rates in the NP state becomes insignificant [Fig. S7(d) in the [supplementary material](#)], highlighting a much weaker correlation between single-electron movements in interacting DDs.

This experiment provides the first explicit measurement of temperature effects on QCA switching operation. At elevated temperatures, where the Coulomb blockade is weakened, we observe degradation in abrupt switching. This degradation would lead to signal loss along a chain of cells unless proper clocking mechanisms are implemented. Clocking mechanisms in QCA are

essential for controlling signal propagation and ensuring reliable operation across different temperatures. These mechanisms modulate the potential barriers between quantum dots within cells, enabling efficient and correct polarization of QCA cells,^{25,26} as experimentally demonstrated in Refs. 27 and 28.

The [supplementary material](#) is provided to support and clarify our experimental and simulation protocols. Section S1 details the device fabrication process. Section S2 describes how the device is modeled in COMSOL. Section S3 explains the MN, which is essential for achieving a high signal-to-noise ratio in gate reflectometry, and discusses how the COMSOL-simulated device is integrated with the MN. Section S4 presents the experimentally measured response of the MN for the double dot D_1D_2 in both blockaded and non-blockaded regimes. Section S5 outlines the biasing scheme for QCA operation, provides a detailed description of the relevant charge configurations, and includes a close-up view of the experimentally observed NP state. Finally, Sec. S6 provides a step-by-step guide to the calculations, enabling a clear comparison between experimental results and theoretical predictions.

This work was supported by the National Science Foundation under Grant No. DMR-1904610. We acknowledge the support of the EU (QuantERA MENTA) and the Spanish MCIU

(Grant No. PID2021-126273NB-I00). The authors thank Daniel Noronha for multiple useful discussions and help with RF board fabrication. All figures were drawn by the authors.

AUTHOR DECLARATIONS

Conflict of Interest

The authors have no conflicts to disclose.

Author Contributions

Alexei O. Orlov: Conceptualization (equal); Data curation (equal); Writing – original draft (equal); Writing – review & editing (equal). **Mohammad Istiaque Rahaman:** Conceptualization (equal); Data curation (equal); Formal analysis (equal); Investigation (equal); Writing – original draft (equal); Writing – review & editing (equal). **Géza Tóth:** Conceptualization (equal); Formal analysis (equal); Writing – original draft (equal); Writing – review & editing (equal). **Gergo P. Szakmany:** Formal analysis (equal); Writing – original draft (equal); Writing – review & editing (equal). **Xavier Jehl:** Validation (equal); Writing – review & editing (equal). **Jonathan D. Chisum:** Validation (equal); Writing – review & editing (equal). **Craig S. Lent:** Funding acquisition (equal); Writing – review & editing (equal). **Gregory L. Snider:** Data curation (equal); Funding acquisition (equal); Investigation (equal); Writing – review & editing (equal).

DATA AVAILABILITY

The data that support the findings of this study are available from the corresponding author upon reasonable request.

REFERENCES

- ¹C. S. Lent, P. D. Tougaw, W. Porod, and G. H. Bernstein, *Nanotechnology* **4**, 49 (1993).
- ²A. O. Orlov, I. Amlani, G. H. Bernstein, C. S. Lent, and G. L. Snider, *Science* **277**, 928–930 (1997).
- ³K. K. Likharev, *IBM J. Res. Dev.* **32**, 144–158 (1988).
- ⁴A. O. Orlov, I. Amlani, G. Toth, C. S. Lent, G. H. Bernstein, and G. L. Snider, *Appl. Phys. Lett.* **73**, 2787–2789 (1998).
- ⁵G. Tóth, A. O. Orlov, I. Amlani, C. S. Lent, G. H. Bernstein, and G. L. Snider, *Phys. Rev. B* **60**, 16906 (1999).
- ⁶H. Grabert and M. H. Devoret, *Single Charge Tunneling Coulomb Blockade Phenomena in Nanostructures*, NATO ASI Series, 294, Series B (Plenum Press, New York, 1991).
- ⁷G. Tóth and C. S. Lent, *J. Appl. Phys.* **89**, 7943–7953 (2001).
- ⁸F. Persson, C. M. Wilson, M. Sandberg, G. Johansson, and P. Delsing, *Nano Lett.* **10**, 953–957 (2010).
- ⁹C. Ciccarelli and A. J. Ferguson, *New J. Phys.* **13**, 093015 (2011).
- ¹⁰M. J. Filmer, T. A. Zirkle, J. Chisum, A. O. Orlov, and G. L. Snider, *Appl. Phys. Lett.* **116**, 213103 (2020).
- ¹¹T. A. Zirkle, M. J. Filmer, J. Chisum, A. O. Orlov, E. Dupont-Ferrier, J. Rivard, M. Huebner, M. Sanquer, X. Jehl, and G. L. Snider, *Appl. Sci.* **10**, 8797 (2020).
- ¹²M. J. Filmer, M. Huebner, T. A. Zirkle, X. Jehl, M. Sanquer, J. D. Chisum, A. O. Orlov, and G. L. Snider, *Sci. Rep.* **12**, 3098 (2022).
- ¹³J. I. Colless, A. C. Mahoney, J. M. Hornibrook, A. C. Doherty, H. Lu, A. C. Gossard, and D. J. Reilly, *Phys. Rev. Lett.* **110**, 046805 (2013).
- ¹⁴N. Ares, F. J. Schupp, A. Mavalankar, G. Rogers, J. Griffiths, G. A. C. Jones, I. Farrer, D. A. Ritchie, C. G. Smith, A. Cottet, G. A. D. Briggs, and E. A. Laird, *Phys. Rev. Appl.* **5**, 034011 (2016).
- ¹⁵F. Ansaloni, A. Chatterjee, H. Bohuslavský, B. Bertrand, L. Hutin, M. Vinet, and F. Kuemmeth, *Nat. Commun.* **11**, 6399 (2020).
- ¹⁶R. Mizuta, R. M. Otxoa, A. C. Betz, and M. F. Gonzalez-Zalba, *Phys. Rev. B* **95**, 045414 (2017).
- ¹⁷N. M. Zimmerman and M. W. Keller, *J. Appl. Phys.* **87**, 8570–8574 (2000).
- ¹⁸T. A. Fulton and G. J. Dolan, *Phys. Rev. Lett.* **59**, 109 (1987).
- ¹⁹COMSOL Multiphysics Reference Manual, Version 6.2, www.comsol.com.
- ²⁰P. Lafarge, H. Pothier, E. R. Williams, D. Esteve, C. Urbina, and M. H. Devoret, *Z. Phys. B* **85**, 327–332 (1991).
- ²¹A. Morello, J. J. Pla, F. A. Zwanenburg, K. W. Chan, K. Y. Tan, H. Huebl, M. Möttönen, C. D. Nugroho, C. Yang, J. A. van Donkelaar, A. D. C. Alves, D. N. Jamieson, C. C. Escott, L. C. L. Hollenberg, R. G. Clark, and A. S. Dzurak, *Nature* **467**, 687–691 (2010).
- ²²C. Wasshuber, H. Kosina, and S. Selberherr, *IEEE Trans. Comput.-Aided Des. Integr. Circuits Syst.* **16**, 937–944 (1997).
- ²³D. Ferry and S. M. Goodnick, *Transport in Nanostructures* (Cambridge University Press, 1999), p. 6.
- ²⁴J. C. Frake, S. Kano, C. Ciccarelli, J. Griffiths, M. Sakamoto, T. Teranishi, Y. Majima, C. G. Smith, and M. R. Buitelaar, *Sci. Rep.* **5**, 10858 (2015).
- ²⁵G. Tóth and C. S. Lent, *J. Appl. Phys.* **85**, 2977–2984 (1999).
- ²⁶C. S. Lent and B. Isaksen, *IEEE Trans. Electron Devices* **50**, 1890–1896 (2003).
- ²⁷A. O. Orlov, R. Kummaruru, R. Ramasubramaniam, C. S. Lent, G. H. Bernstein, and G. L. Snider, *J. Nanosci. Nanotechnol.* **2**, 351–355 (2002).
- ²⁸Y. Tang, A. O. Orlov, G. L. Snider, and P. J. Fay, *Appl. Phys. Lett.* **95**, 193109 (2009).